Advances in Natural Sciences:
Nanoscience and Nanotechnology

PAPER

Photocatalytic properties of nanosized zinc ferrite and zinc chromite

Adv. Nat. Sci.: Nanosci. Nanotechnol. **12** (2021) 015004 (9pp) https://doi.org/10.1088/2043-6254/abde3b

Photocatalytic properties of nanosized zinc ferrite and zinc chromite

N P Shabelskaya[1], M A Egorova[1], E V Vasileva[1] and O E Polozhentsev[2]

[1] Platov South-Russian State Polytechnic University (NPI), Russia
[2] Southern Federal University, Russia

E-mail: nina_shabelskaya@mail.ru

Received 20 July 2020
Accepted for publication 27 September 2020
Published 4 February 2021

Abstract

A simple one-step synthesis of developed surface zinc ferrite is proposed (S_{BET} = 453.1 m^2 g^{-1}). The formation of zinc ferrite, zinc chromite (S_{BET} = 53.6 m^2 g^{-1}), and mixed zinc ferrite-chromite (S_{BET} = 37.4 m^2 g^{-1}) structures is studied. The resulting materials are analysed using x-ray phase and x-ray fluorescence analysis, IR spectrometry, electron microscopy, TGA and BET method. Single-phase sample formation mechanism is proposed, which includes transition element cation chelate complex formation stage in the presence of citric acid and subsequent thermal decomposition of the complexes formed. The synthesised materials exhibited photocatalytic activity in the decomposition of an organic dye under the action of hydrogen peroxide. The highest catalytic activity is demonstrated by zinc ferrite in acidic medium; the calculated reaction rate constant is 0.010 min^{-1} for $ZnFe_2O_4$, 0.008 min^{-1} for $ZnFeCrO_4$, 0.007 min^{-1} for $ZnCr_2O_4$. The results can be applied to obtain materials suitable for wastewater treatment processes at industrial enterprises where organic dyes are used in production cycles.

Keywords: zinc ferrite, zinc chromite, nanostructured materials, oxidative degradation of dye, aqueous solutions purification
Classification numbers: 2.03, 5.06, 5.07

1. Introduction

Oxide compounds of transition metals are in focus of intensive research due to their successful combination of a number of important technical properties. Zinc ferrites and zinc chromites are widely used as sensors to detect hydrogen sulphide [1], acetone [2], ethylene glycol [3], as electrodes of lithium batteries [4, 5], as catalysts for ammonium perchlorate decomposition [6], tetracycline chloride decomposition [7], methane combustion [8], to reduce carbon dioxide emissions [9], they also exhibit antibacterial properties [10, 11]. Widely discussed in the scientific literature is the phenomenon of photocatalytic activity established for zinc ferrite and zinc chromite for a number of important reactions [12–20]. In particular, zinc ferrite is used to purify aqueous solutions of organic pollutants: methylene blue [12–14], rhodamine B [12, 15], acid blue [16], methyl orange [13, 17–19], Congo red [20]. Systems based on zinc compounds exhibit high photocatalytic activity in the process of organic dye removal. For zinc ferrite [21], the calculated reaction rate constant is 0.0085 min^{-1} with the dye removal efficiency of 98%. The NiO-ZnO oxide system [22] makes it possible to remove 100% of the dye from an aqueous solution within 170 min. As a rule, composite materials produced lead to the catalytic activity increase in comparison with the activity of starting materials. For example, as shown in [23], the introduction of 9% to 50% TiO_2 to $ZnFe_2O_4$ leads to the organic dye destruction degree increase from 70% to 98%, while zinc ferrite and titanium (IV) oxide separately exhibits a noticeably lower catalytic activity. Similar data were obtained for the $ZnCr_2O_4/TiO_2$ system [11]. Produced composite materials based on zinc and silver oxide compounds [22, 24], as a rule, also improve the catalytic activity. Doping composite materials with organic additives, for example, $ZnFe_2O_4/g\text{-}C_3N_4$, 15 wt.% lead to a significant increase in the reaction rate [21] to 0.1955 min^{-1}. One of the rapidly developing areas of oxide spinel chemical technology is the development of nanostructured material synthesis methods. Ceramics is considered to be the traditional method of spinel synthesis, during which high-temperature firing of the initial precursors, customarily an oxide, is used [25, 26]. Sometimes, to reduce synthesis temperature or duration, a combination of solid-state and

additional methods such as microwave irradiation [27] and hydrothermal exposure [28] is used. Solvothermal [29] and, as a special case, hydrothermal [30] methods, sol-gel technology [10, 31], and organic precursor synthesis [14, 19, 23, 32–34] are usually used to synthesise fine crystalline materials. Urea [23], citric acid [33], ascorbic acid [34], sugarcane [14], plant leaf extract [30, 35, 36], and agar-agar [19] can be used as templates.

Despite sufficient knowledge about zinc ferrite-chromite system compounds, the mechanism of material structure formation is not fully understood. The aim of the present study is to investigate the formation processes of synthesised zinc ferrite and zinc chromite structures, their morphological features and catalytic activity in the processes of methyl orange oxidative decomposition in the presence of hydrogen peroxide.

2. Experiment

2.1. Materials

The following starting materials of analytical grade are used: zinc nitrates $Zn(NO_3)_2 \cdot 6H_2O$, iron (III) nitrates $Fe(NO_3)_3 \cdot 9H_2O$, chromium (III) sulfate $Cr_2(SO_4)_3 \cdot 18H_2O$ (component content is no less than 99%), 25% (mass.) ammonia solution $NH_3 \cdot H_2O$, and citric acid $C_6H_8O_7$.

2.2. Zinc ferrite-chromite synthesis

For the synthesis of materials, a technique similar to that described in [37] was used, the only difference was that citric acid was used as an organic precursor. In a typical procedure, 1 mol/l solutions of zinc nitrate, iron (III) nitrate, and chromium (III) sulfate were used. To prepare the solutions, zinc nitrate $Zn(NO_3)_2 \cdot 6H_2O$, iron (III) nitrate $Zn(NO_3)_2 \cdot 6H_2O$, and chromium (III) sulfate $Cr_2(SO_4)_3 \cdot 18H_2O$ were dissolved in distilled water, measured in accordance with the recipe. Salt solutions were measured with a graduated cylinder and placed in a stainless steel reaction vessel. Aqueous ammonia solution was added at vigorous mixing, and formation of a coloured flocculent precipitate was observed. Then, citric acid solution was added to the resulting suspension, while mixing was continued. A clear, coloured solution was obtained, which was heated until the liquid completely evaporated. In this case, a viscous gel-like substance was formed, which gradually transformed into a solid porous material. With further heating, an intensive decomposition process took place, accompanied by gaseous substance release and by reaction system luminescence. Heating was continued until the organic component completely decomposed. Samples containing Cr were additionally subjected to heat treatment for 30 min at a temperature of 1073 K and a heating rate of 13 K min^{-1}.

2.3. Characteristics

Phase composition was studied by point scanning method (at 0.01° step, and 2 s. accumulation time) in the range of 2θ from 15° to 70° using ARL X'TRA x-ray diffractometer (monochromatised Cu-Kα radiation was used). Qualitative phase composition was determined using PDF-2 in the Crystallographica software package. Crystallite size calculation was carried out with Scherrer equation according to the following formula (1):

$$D = 0.94 \times \lambda/(B \times \cos\theta), \quad (1)$$

where D is the average crystal size, nm; λ is the x-ray wavelength, nm; B is the peak line width at half of its height; cos θ is the peak angle cosine. The surface area was determined using ChemiSorb 2750 B apparatus. Physical nitrogen adsorption isotherms were obtained at 77 K. Before the measurement, the samples were degassed. The composition was refined on the x-ray Fluorescence M4 TORNADO (BRUKER). The test area of the sample was measured at 20 points with an exposure of 20 s per point. The thermogravimetric analysis was carried out on NETZSCH STA 449F5 STA449F5 using ~10 mg of powders at a heating rate of 10 K min^{-1} in the temperature range of 333–873 K. Samples' IR absorption spectra were obtained using Varian 640 IR-Fourier spectrometer (USA) with the method of impaired total internal reflection, the prism material was diamond. Samples were prepared by pressing with potassium bromide (1% (mass). Samples' micrographs were obtained using Quanta 200 scanning electron microscope. Images were taken at accelerating voltage of up to 30 kV.

2.4. Photocatalytic activity analysis

Catalytic activity of the synthesised materials was studied using a model solution of methyl orange ($\lambda_{max} = 465$ nm) with the concentration of 40 mg/l. The preparation procedure was as follows: 10 ml of the organic dye initial solution was placed in a quartz reaction vessel; 10–12 mg of catalyst and 10 ml of 3% (mass.) hydrogen peroxide solution were added. The concentration of the dye in the solution was determined by the photocolorimetric method using KFK-2-UHL 4.2 device at certain time intervals. The photocatalytic organic dye decomposition experiment was conducted in an in-house-made photocatalytic reaction system. A 100 W JC halogen lamp (Camelion, Camelion International Ltd, China) was used as the light source. The distance from the light source to the reaction system surface was 50 mm. Before the start of the experiment, the reaction system was thoroughly mixed, insulated from light for 0.5 h to attain the adsorption/desorption equilibrium. The degree of catalytic destruction (P) of methyl orange was calculated with the following formula (2):

$$P = C/C_0, \quad (2)$$

where C_0 is the initial concentration of the solution, mg l^{-1}; C is the current concentration of the solution, mg l^{-1}. To create certain medium acidity, 1 mol l^{-1} sulfuric acid and sodium alkali solution was used.

2.5. Recycling

When the experiment was over, the catalyst was separated by decantation, washed 3 times with distilled water, and dried at room temperature; and its catalytic activity was re-studied as described in 2.4.

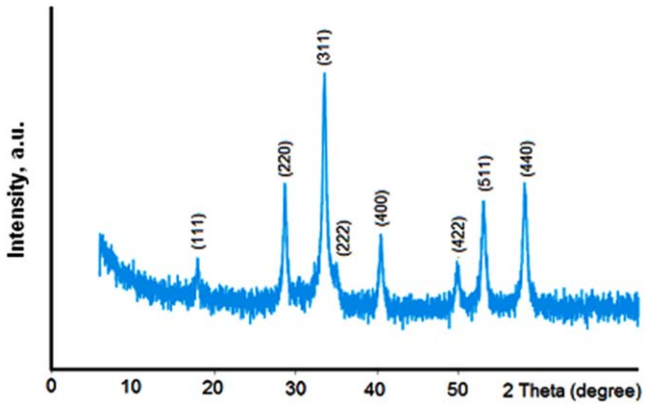

Figure 1. X-ray diffraction pattern of $ZnFe_2O_4$ sample.

3. Results and discussion

3.1. Sample structure and morphological features analysis

In all cases studied, synthesised materials had porous structure. Figures 1–3 show x-ray diffraction patterns of the synthesised samples. Zinc ferrite x-ray diffraction pattern (figure 2) after thermolysis contains only lines characterising the cubic spinel phase $ZnFe_2O_4$ (PDF Number 010-70-6490, the most intense lines have indices of (311), (220), (440)). The X-ray diffraction patterns of zinc chromite and mixed zinc ferrite-chromite (figures 2(a) and 3(a)) after thermolysis contain zinc sulfate monohydrate $ZnSO_4{\cdot}H_2O$ (PDF Number 000-12-0781) in addition to $ZnCr_2O_4$ spinel (PDF Number 010-75-4052, the most intense lines have indices of (311), (220), (440)). To obtain a single-phase material, these samples were subjected to additional heat treatment. As a result, single-phase samples with cubic spinel structure $ZnCr_2O_4$ (PDF Number 010-75-4050), zinc chromium iron oxide (PDF Number 010-79-5287) are formed (figures 2(b) and 3(b)).

After thermolysis, porous materials are formed (figures 4(a)–(c)). The array parameter values, average crystallite size (calculated by the Debye-Scherrer method), and the surface area determined by BET method are given in table 1. Figure 5 and table 1 show data on the study of the elemental composition of samples.

Figure 6 shows the TGA data. According to the results obtained (figure 6, curves 1, 3, 5), the mass loss of samples in the range of 33-873 K does not exceed 10%, which may indicate the absence of an organic component in the samples.

Zinc ferrite and zinc chromite formation processes can be represented consisting of a number of stages. Transition element cations are present in the solution as a result of starter salt dissociation according to (3)–(5) equations in the presence of ammonia solution, hydroxides of the corresponding metals are precipitated (equations (6)–(8)):

$$Zn(NO_3)_2 = Zn^{2+} + 2NO_3^-, \quad (3)$$

$$Fe(NO_3)_3 = Fe^{3+} + 3NO_3^-, \quad (4)$$

$$Cr(NO_3)_3 = Cr^{3+} + 3NO_3^-, \quad (5)$$

$$Zn^{2+} + 2OH^- = Zn(OH)_2, \quad (6)$$

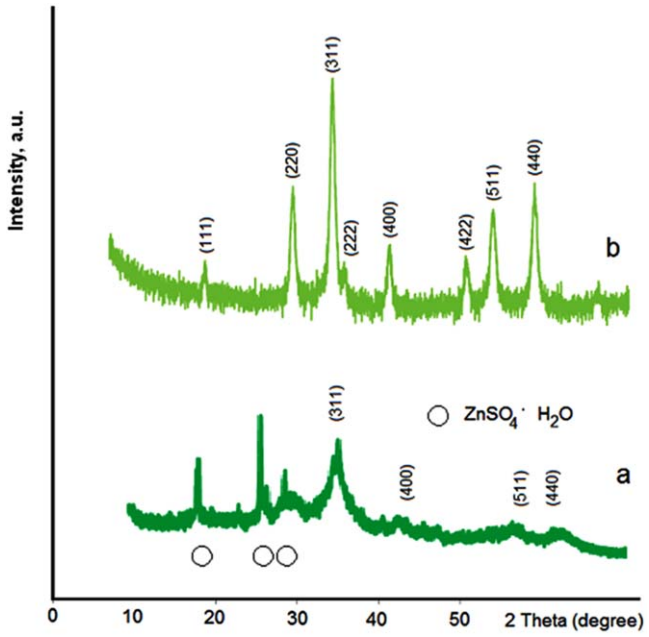

Figure 2. X-ray diffraction pattern of the $ZnFe_{0,6}Cr_{1,4}O_4$ sample. Spinel lines are indexed.

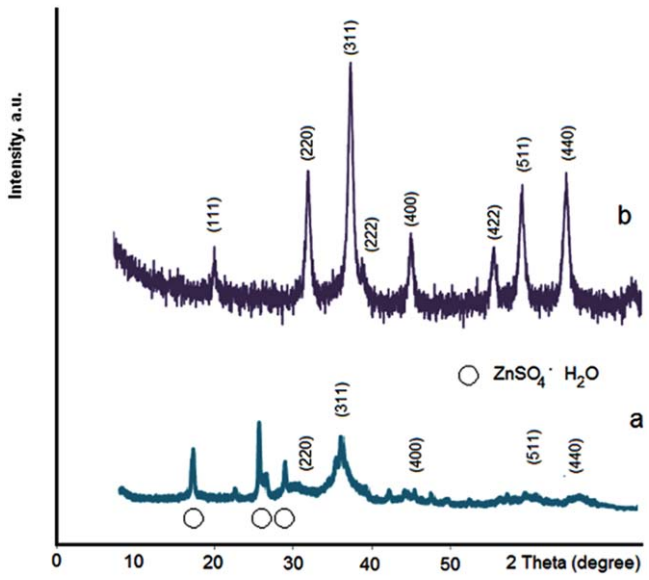

Figure 3. X-ray diffraction pattern of the $ZnCr_2O_4$ sample. Spinel lines are indexed.

$$Fe^{3+} + 3OH^- = Fe(OH)_3, \quad (7)$$

$$Cr^{2+} + 3OH^- = Cr(OH)_3. \quad (8)$$

Hydroxides of all the elements under consideration are amphoteric in nature, which can lead to the process complication which is accompanied by parallel reactions of anionic complex formation:

$$Zn(OH)_2 + 2OH^- = [Zn(OH)_4]^{2-},$$

$$Fe(OH)_3 + 3OH^- = [Fe(OH)_6]^{3-}, ,$$

$$Cr(OH)_3 + 3OH^- = [Cr(OH)_6]^{3-}.$$

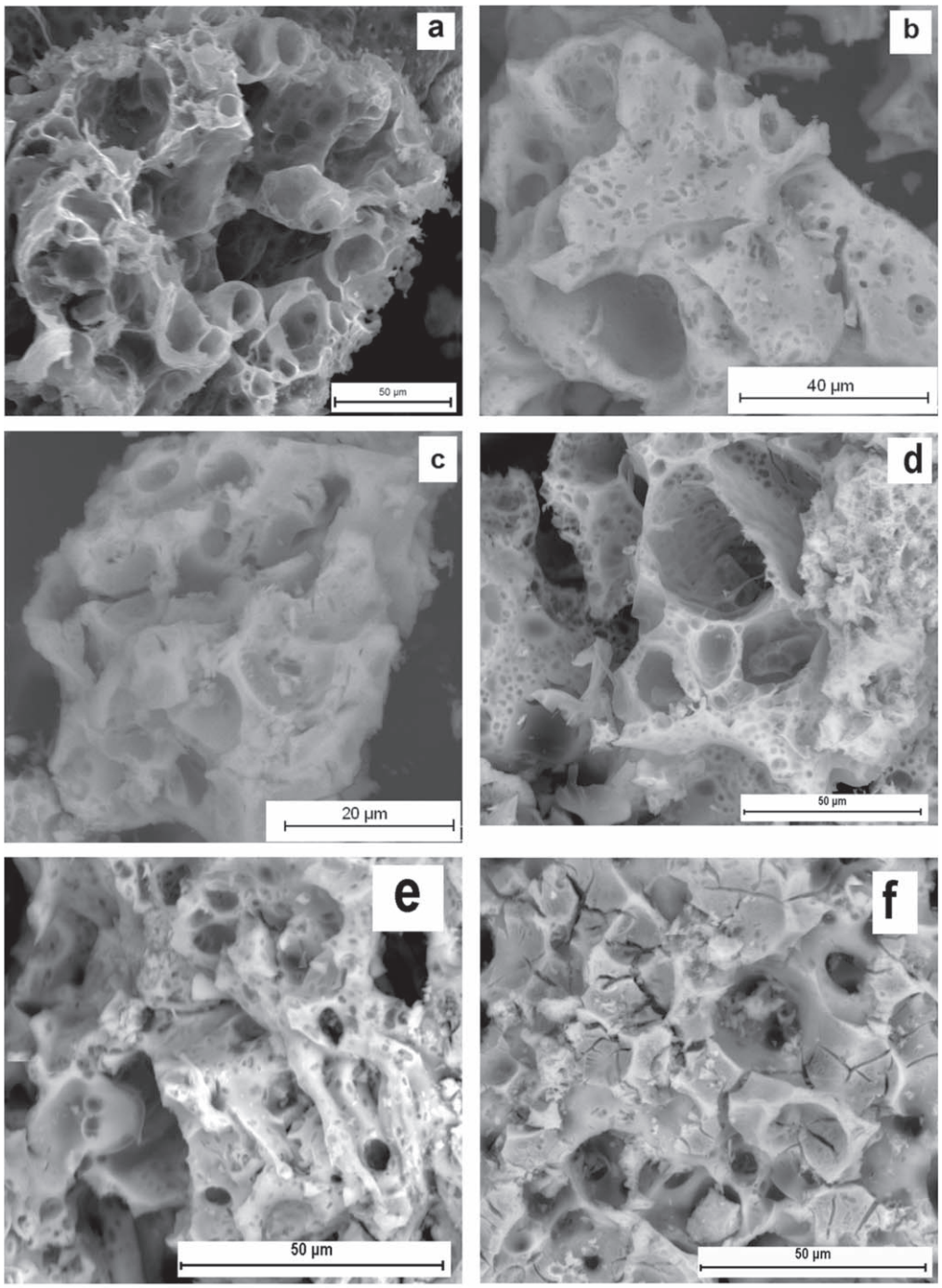

Figure 4. SEM-images of synthesised materials, (a)–(c) starting materials, (d)–(f) materials after catalysis: (a), (d) zinc ferrite, (b), (e) mixed zinc ferrite-chromite, (c), (f) zinc chromite.

Table 1. Array parameters (a), average crystal size (D), compound and surface area values (S_{BET}) of $ZnFe_{2-x}Cr_xO_4$ spinel ($x = 0.0, 1.4, 2.0$).

				Atom. C [at.%] (K-series)		
Sample	a, nm	D, nm	S_{BET}, $m^2\ g^{-1}$	Zn	Fe	Cr
$ZnFe_2O_4$	0.8441	3.2	453.1	39.13	60.87	—
$ZnFe_{0.6}Cr_{1.4}O_4$	0.8346	3.7	37.4	37.87	15.28	46.85
$ZnCr_2O_4$	0.8333	2.5	26.8	37.46	—	62.54

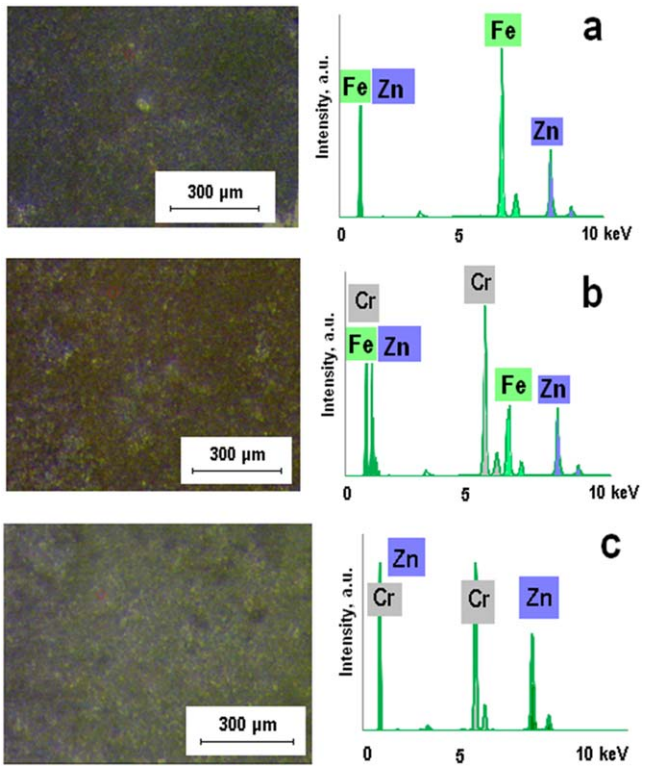

Figure 5. X-ray fluorescence analysis data of synthesised materials: (a) zinc ferrite, (b) mixed zinc ferrite-chromite, (c) zinc chromite.

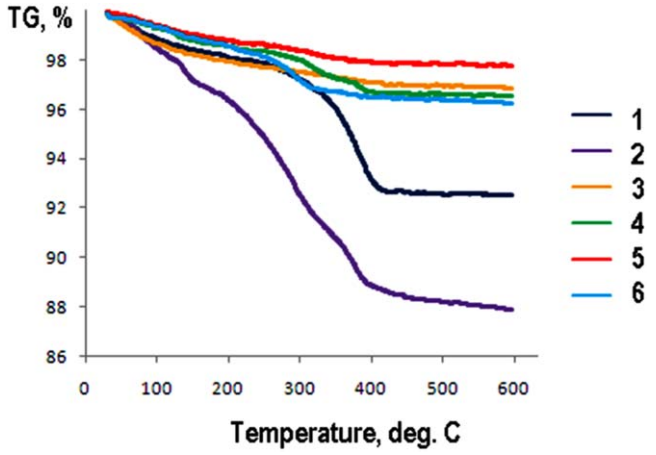

Figure 6. TGA data of synthesised materials: (1), (2) zinc ferrite, (3), (4) mixed zinc ferrite-chromite, (5), (6) zinc chromite. Data before (1), (3), (5) and after (2), (4), (6) catalysis.

When citric acid is introduced into the reaction system, citrate formation is possible according to the following reactions:

$$Zn(OH)_2 + C_6H_8O_7 = Zn(C_6H_6O_7) + 2H_2O,$$
$$Fe(OH)_3 + C_6H_8O_7 = Fe(C_6H_5O_7) + 3H_2O,$$
$$Cr(OH)_3 + C_6H_8O_7 = Cr(C_6H_5O_7) + 3H_2O,$$
$$[Zn(OH)_4]^{2-} + 2C_6H_6O_7^{2-} = [Zn(C_6H_6O_7)_2]^{2-},$$
$$[Fe(OH)_4]^{2-} + 3C_6H_6O_7^{2-} = [Fe(C_6H_6O_7)_3]^{3-},$$
$$[Cr(OH)_4]^{2-} + 3C_6H_6O_7^{2-} = [Cr(C_6H_6O_7)_3]^{3-},$$

with the subsequent formation of chelate complexes of volumetric structure.

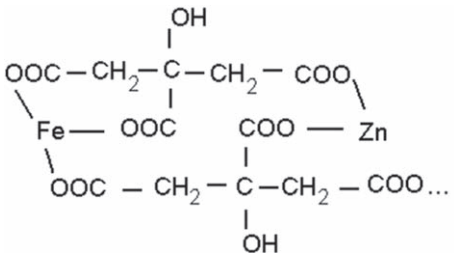

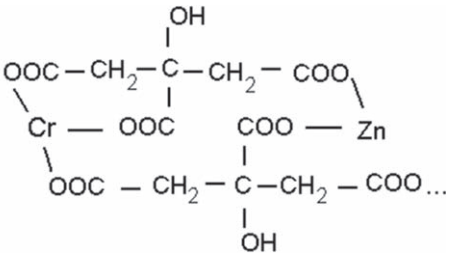

When heated, the complex decomposition occurs and dispersed spinel powder is formed, whose composition is $ZnFe_2O_4$, $ZnFe_{0.6}Cr_{1.4}O_4$ and $ZnCr_2O_4$. In this case, the effect of the precursor form inheritance is observed; a similar phenomenon was observed earlier, for example, in [38]. In the presence of chromium (III) sulfate in the system, the reactions are observed as described by equations (3)–(8) and by the following equations:

$$Cr_2(SO_4)_3 = 2Cr^{3+} + 3SO_4^{2-},$$
$$Cr^{3+} + 3OH^- = Cr(OH)_3.$$

Apparently, during the sample structure formation, zinc sulfate is also formed according to the following equation:

$$Zn^{2+} + SO_4^{2-} = ZnSO_4.$$

Based on the obtained experimental data, it is concluded that the reaction system temperature is not sufficient for $ZnSO_4$ decomposition, and that zinc sulfate is part of the synthesis product. During the final annealing, zinc sulfate decomposes with the formation of ZnO oxide, which is part of single-phase cubic spinel structure. According to the XRD data, zinc ferrite and zinc chromite samples are formed in cubic spinel structure. As it can be seen from the data provided in table 2, for zinc chromite and mixed zinc ferrite-chromite, S_{BET} values are lower than those for $ZnFe_2O_4$. This may be due to additional heat treatment of the material that leads to crystallinity degree increase. Higher *D* values for zinc ferrite can be associated with the formation of clusters (in figure 4(a), particles of complex shape are seen to form). IR-spectroscopy results (figure 7) supplement material structure data.

Table 2. Synthesised material composition.

#	Zn_A	Zn_B	Fe_A	Fe_B	Cr_B	$(Fe,Cr)_{B/A}$	Composition[a]
1	204	6	30	417	—	0.07	$(Zn_{0.93}Fe_{0.07})[Zn_{0.07}Fe_{1.84}]O_4$
2	343	5	18	56	432	0.04	$(Zn_{0.96}Fe_{0.04})[Zn_{0.04}Fe_{0.56}\ Cr_{1.4}]O_4$
3	270	—	—	—	555	0	$(Zn)[Cr_2]O_4$

[a] Cations in tetra-positions of spinel structure are shown in parentheses; cations in octa-positions are shown in square brackets

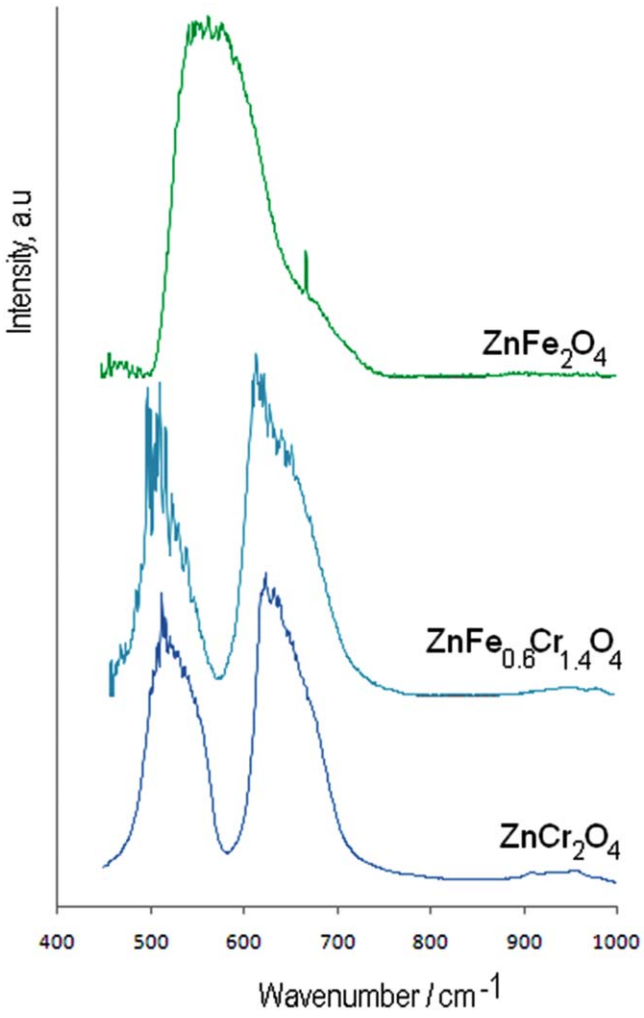

Figure 7. IR absorption spectra.

Based on the assumption that the vibration of the higher valence cation corresponds to the most intense spectral band [23, 39], it can be assumed that the peaks of 565-670 cm^{-1} correspond to vibrations of chromium and iron trivalent cations. The 512 cm^{-1} line characterises the vibrations of bivalent zinc cation. Small peaks of 470 cm^{-1} can be attributed to vibrations of zinc cations in octahedral positions. Zinc chromite ($ZnCr_2O_4$) crystallises in normal spinel structure, with zinc cation placement in tetra-positions, and chromium cations - in octa-positions. For the sample in figure 7, the 512 cm^{-1} line can be attributed to the vibrations of zinc cations in terta-positions; the 623 cm^{-1} line – to the vibrations of Cr^{3+} cation in octa-positions of spinel array. For zinc ferrite, the nature of IR-spectrum is significantly different.

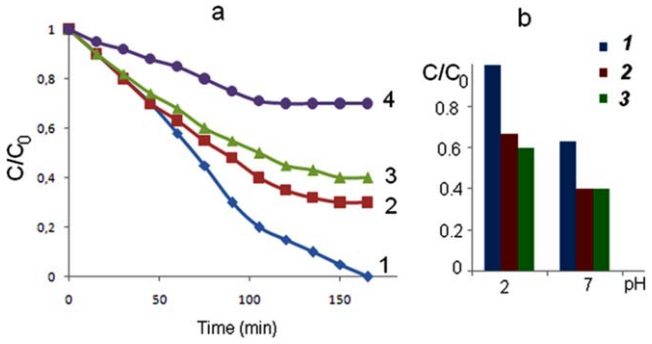

Figure 8. Methyl orange decomposition degree dependence on the reaction time (a) and on medium acidity (b) in the presence of $ZnFe_2O_4$ (1), $ZnFe_{0.6}Cr_{1.4}O_4$ (2), $ZnCr_2O_4$ (3), no catalyst (4).

Apparently, this is due to a higher degree of reversal [40] of the formed spinel. This is evidenced by a weak peak in the region of 668 cm^{-1} and the peak split in the region of 510-570 cm^{-1}. Quantitative estimate of the cation content in octa- and tetra-positions of the spinel structure is given in table 2.

3.2. Catalytic activity analysis

The catalytic activity of the synthesised materials is studied using the example of methyl orange oxidative destruction in the presence of hydrogen peroxide. The time ratio depends on methyl orange amount that undergoes catalytic destruction as shown in figure 8(a).

To study the effect of medium acidity, sulfuric acid solution was additionally introduced into the reaction system to reach pH 2, and sodium hydroxide was additionally introduced into the reaction system to reach pH 7. In the course of synthesised materials analysis, their high catalytic activity is established. Zinc ferrite acts as the most active catalyst for the organic dye decomposition under the influence of H_2O_2: during the process at pH 2, 100% dye removal from the solution was observed after 165 min from the start of the reaction. For zinc chromite, under given conditions, 60% dye removal was observed (figure 8). Mixed zinc ferrite-chromite exhibits intermediate activity; the maximum degree of dye destruction under given conditions was 70%. Reaction medium acidity increase leads to catalytic activity decrease in all materials (figure 8(b)). Figures 4(d)–(f) depict photomicrographs of the material after the catalysis process. It should be noted that there is no significant change in the morphology of the samples. The calculated reaction rate constant is 0.010 min^{-1} for $ZnFe_2O_4$, 0.008 min^{-1} for $ZnFeCrO_4$, and 0.007 min^{-1} for $ZnCr_2O_4$. Figure 6 (curves 2, 4, 6) shows the TGA data after the catalysis process. There

was an increase in the mass loss of samples compared to samples before catalysis by 0.4%-4.6%. This result may be related to the adsorption of an organic dye on the surface of the catalyst. The synthesised materials exhibit high catalytic activity and operational stability in comparison with similar catalytic systems. For example, in [22] it was shown that the use of the NiO-ZnO system resulted in 100% dye removal from the aqueous solution within 170 min The Ag-doped ZnO-based catalyst exhibited higher activity in this process (the dye removal rate constant was 0.02789 min^{-1}); however, such a catalyst system has higher cost due to the expensiveness of silver. A similar system (with the addition of 1 wt% GO) turns out to be less active (the reaction rate constant is 0.005 min^{-1} [24]). In [24], the $ZnFe_2O_4/ZnO/4$ wt% GO system was considered, which was highly active in methylene blue decomposition (the reaction rate constant was 0.033 min^{-1}). For the $ZnCr_2O_4/TiO_2$ system [11] in the process of purifying an aqueous solution from methylene blue, the result of 120 min was obtained. The decrease in the dye decomposition time can be associated with the synergistic effect of d-element oxide forms. In [23], the use of a composite material ($ZnFe_2O_4/TiO_2$ ($wTiO_2 = 25\%$)) leads to solution purification in 4 h, which is more than 1.4 times slower than the result obtained in this study for $ZnFe_2O_4$. Reaction rate and depth increase in cases of zinc ferrite and mixed zinc ferrite-chromite can be associated with the Fenton system formation Fe^{3+}/Fe^{2+} during the redox process:

$$Fe^{3+} + H_2O_2 + 2H^+ = Fe^{2+} + 2H_2O.$$

The mechanism of organic dye decomposition by hydrogen peroxide has been discussed in a number of publications [22, 23, 33, 39, 41, 42]. A possible reaction mechanism can be represented as follows. Under the influence of radiation, hydrogen peroxide decomposes on the catalyst surface (figure 9).

$$H_2O_2 + h\nu \rightarrow O^0 + H_2O.$$

During the reaction, active molecular oxygen is formed, which decomposes the organic dye molecule:

$$O^0 + MO \rightarrow \text{Intermediates} \rightarrow CO_2 + H_2O + \ldots$$

In case of zinc ferrite and zinc ferrite-chromite, the reaction proceeds (figure 10).

$$ZnFe_2O_4 + h\nu \rightarrow (ZnFe^{3+}Fe^{2+}O_4)^-.$$

A similar process mechanism was considered in [23]. It is assumed that $Fe^{3+} \rightarrow Fe^{2+}$ transition will occur more easily in case of Fe^{3+} cation presence in tetra-positions of the spinel structure. This becomes evident due to the experimentally observed fact of sample catalytic activity increase when the spinel reversal degree increases.

$$(ZnFe^{3+}Fe^{2+}O_4)^- + H_2O_2 \rightarrow ZnFe_2O_4 + O^0 + H_2O.$$

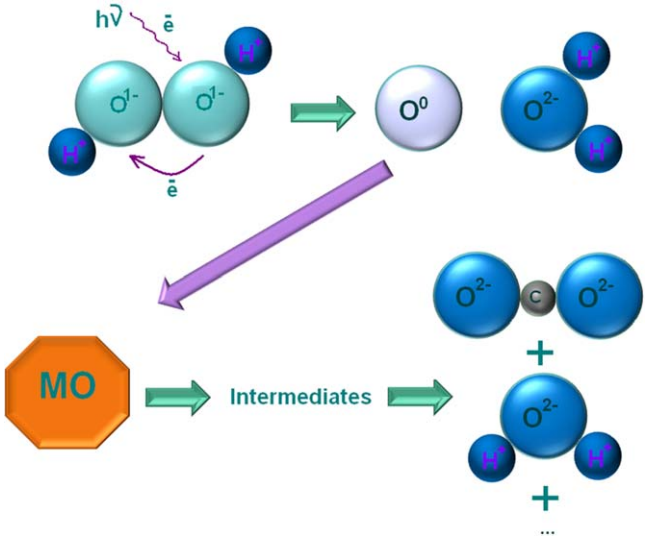

Figure 9. Possible decomposition mechanism involving $ZnCr_2O_4$.

Next, the process of dye destruction is observed:

$$O^0 + MO \rightarrow \text{Intermediates} \rightarrow CO_2 + H_2O + \ldots$$

In acidic medium, equilibrium (9) is observed to shift to the left and cations become available for the process of $Fe^{3+} \rightarrow Fe^{2+}$:

$$Fe^{3+} \cdot H_2O + H_2 \rightleftarrows (FeOH)^{2+} + (H_3O)^+. \quad (9)$$

In alkaline medium, equilibrium (9) is observed to shift to the right due to the protolysis reaction, which probably complicates iron cation reduction.

At the end of the reaction, the catalytically active materials are re-examined. Without a decrease in activity, $ZnFe_2O_4$ samples withstand 5 consecutive cycles of use.

The results can be useful for selecting materials that are promising for wastewater treatment systems at industrial enterprises that use organic dyes in their production cycles.

4. Conclusion

Spinel structure formation process for zinc ferrite and zinc chromite of $ZnFe_{2-x}Cr_xO_4$ ($x = 0.0,\ 1.4,\ 2.0$) composition is investigated. It is found that the use of the sol-gel technique in the presence of citric acid as a template makes it possible to synthesise a developed surface zinc ferrite ($S_{BET} = 453.1\ m^2\ g^{-1}$). Chromium-containing systems require additional heat treatment, which leads to surface area decrease ($S_{BET} = 53.6\ m^2\ g^{-1}$ for zinc chromite, and $S_{BET} = 37.4\ m^2\ g^{-1}$ for mixed zinc ferrite-chromite). The mechanism of single-phase samples formation includes the stage of cation chelate complex formation for transition elements and citric acid, and their subsequent thermal decomposition. The synthesised materials exhibit photocatalytic activity during the decomposition of methyl orange with hydrogen peroxide. The highest reaction rate was observed for zinc ferrite in pH = 2. The calculated reaction rate constant is 0.010 min^{-1} for $ZnFe_2O_4$, 0.008 min^{-1} for $ZnFeCrO_4$,

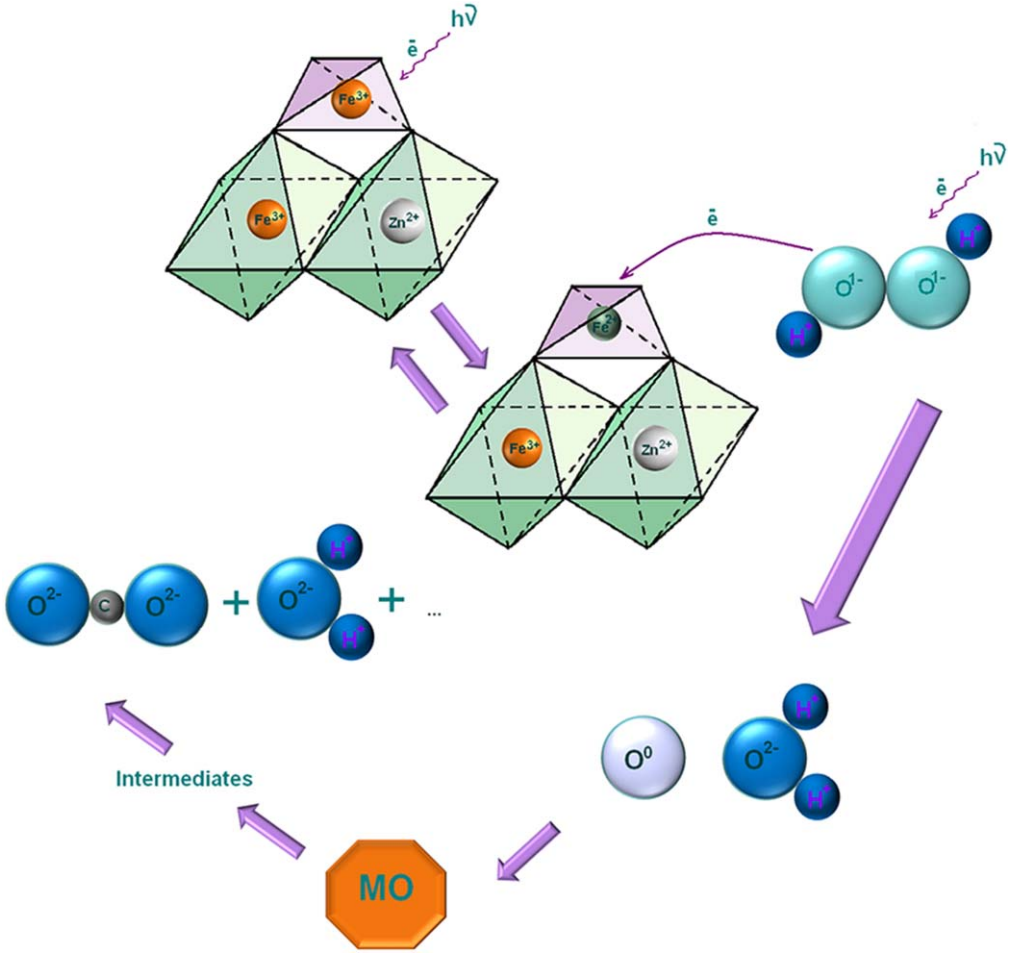

Figure 10. Possible decomposition mechanism involving $ZnFe_2O_4$ or $ZnFe_{0.6}Cr_{1.4}O_4$.

$0.007min^{-1}$ for $ZnCr_2O_4$. A possible reaction mechanism is proposed in the presence of zinc chromite and zinc ferrite (or mixed ferrite-chromite). The results can be used to obtain materials suitable for wastewater treatment processes at industrial enterprises that use organic dyes in their production cycles.

Acknowledgments

The authors are grateful to the staff of Platov South-Russian State Polytechnic University (NPI) Collective Use Center, namely, to Dr A N Saliev for his help in collecting and decoding x-ray data, E N Voloshina for her help in collecting IR spectra data, Dr S I Sulima for her help in BET method samples analysis, and A N Yatsenko for his help in performing microscopic studies.

References

[1] Hai-Jun Z, Fan-Na M, Li-Zhu L, Yu-Jin C and Pin-Jie W 2018 *J. Alloys Compd.* **764** 147
[2] Chu X F, Dai P, Liang S M, Bhattacharya A, Dong Y P and Epifani M 2019 *Phys. E: Low-Dimensional Sys. Nanostruct.* **106** 326
[3] Yang H R, Bai X J, Hao P, Tian J, Bo Y Y, Wang X Z and Liu H 2019 *Sensors and Actuators B: Chem.* **280** 34
[4] Chang L, Tao P, Chunlei W, Yang L, Hailong Y and Yongsong L 2017 *J. Alloys Compd.* **720** 86
[5] Zhibo F, Lening Z, Hui Q, Huijuan Y, Tong Z, Xiaosen Z, Gang C, Yingjin W, Chunzhong W and Dong Z 2018 *J. Alloys Compd.* **762** 480
[6] Wang W R, Guo S S, Zhang D X and Yang Z 2019 *J. of Saudi Chem. Soc* **23** 133
[7] Pang Y X, Kong L J, Lei H Y, Chen D Y and Yuvaraja G 2018 *J. of the Taiwan Inst. of Chem. Eng.* **93** 397
[8] Huang W, Zha W, Zhao D and Feng S 2019 *Solid State Scien.* **87** 49
[9] Xiao J, Yang W Y, Gao S, Sun C X and Li Q 2018 *J. Mat. Scien. & Techn.* **34** 2331
[10] Sharma R P, Raut S D, Jadhav V V, Kadam A S and Mane R S 2019 *Mat. Lett.* **237** 165
[11] Salehi M, Eshaghi A and Tajizadegan H 2019 *J. All. Comp.* **778** 148
[12] Ghobadifard M, Farhadi S and Mohebbi S 2019 *Res. on Chem. Intermed.* **45** 379
[13] Kharazi P, Rahimi R and Rabbani M 2018 *Mat. Res. Bull.* **103** 133
[14] Patil S B, Naik H S B, Nagaraju G, Viswanath R, Rashmi S K and Kumar M V 2018 *Mat. Chem. And Phys.* **212** 351
[15] Cai A J, Guo A Y, Du L Q, Chang Y F and Wang X P 2018 *JOM* **70** 2169
[16] Salla S, Ankem N R, Kumar P S, Renita A A and Micheal K 2019 *Desalinat. and Water Treatm.* **137** 395

[17] Li Z Z, Chen H B and Liu W X 2018 *Catalysts.* **8** 557
[18] Ma Y, Wang Q and Xing S T 2018 *J. Coll. Interface Scien.* **529** 247
[19] Cherif K, Rekhila G, Omeiri S, Bessekhouad Y and Trari M 2019 *J. Photochem. & Photobiol. A: Chem.* **368** 290
[20] Behera A, Kandi D, Majhi S M, Martha S and Parida K 2018 *J. Nanotechnol.* **9** 436
[21] Renukadevi S and Pricilla A 2020 *Inorgan. Chem. Commun.* **118** 108047
[22] Shena R, Jiang C, Xiang Q, Xie J and Li X 2019 *Appl. Surf. Scie.* **471** 43–87
[23] Xu Q, Feng J, Li L, Xiao Q and Wang J 2015 *J. Alloys Compd.* **641** 110
[24] Li X, Shena R, Mab S, Chenc X and Xiea J 2018 *Appl. Surf. Scie.* **430** 53–107
[25] Koga Y, Okada R, Kobayashi S, Yamada H and Watanabe T 2019 *J. Magn. Magnet. Mat.* **476** 464
[26] Granone L I, Ulpe A C, Robben L, Klimke S, Jahns M, Renz F, Gesing T M, Bredow T, Dillert R and Bahnemann D W 2018 *Phys. Chem. Chem. Phys.* **20** 28267
[27] Litvishkov Y N, Zul'fugarova S M, Aleskerova Z F, Gasangulieva N M, Shakunova N V and Aleskerov A G 2018 *Russ. J. Appl. Chem.* **91** 793
[28] Qu F D, Shang W N, Thomas T, Ruan S P and Yang M N 2018 *Sensors And Actuators B: Chem.* **265** 625
[29] Yu M, Huang Y, Wang K, Han X P, Wang M Y, Zhu Y D and Liu L 2018 *Appl. Surf. Scien.* **462** 955
[30] Nguyen Van C H, Nguyen H K, Huynh H Q, Pham H A, Dinh T M, Luong H N, Phan B T, Tran C K and Dang V Q 2020 *Adv. Nat. Scie.: Nanoscience and Nanotechnology* **11** 015002
[31] Yiqin G, Yadan G, Dandan T, Yuanyuan L, Xuegang W, Peng L and Guanghui W 2019 *J. Alloys Compd.* **781** 1101
[32] Liu P X, Ren Y M, Ma W J, Ma J and Du Y C 2018 *Chem. Eng. J.* **345** 98
[33] Habibi M H and Habibi A H 2014 *J. Industr. Eng. Chem.* **20** 2964
[34] Zhang J, Song J-M, Niu H-L, Mao C-J, Zhang S-Y and Shen Y-H 2015 *Sens. Actuat.* B **221** 55
[35] Bera D, Pal K, Mondal D, Karmakar P, Das S and Nandy P 2020 *Adv. Nat. Scie.: Nanoscience and Nanotechnology* **11** 035015
[36] Parekh K, Nair J and Bhardwaj A 2020 *Adv. Nat. Scie.: Nanoscience and Nanotechnology* **11** 035014
[37] Shabel'skaya N P 2014 *Inorg. Mat.* **50** 1114
[38] Krasil'nikov V N, Gyrdasova O L and Bazuev G V 2008 *Russ. J. Inorg. Chem.* **53** 1854
[39] Arimi A, Megatif L, Granone L I, Dillert R and Bahnemann D W 2018 *J. Photochem. Photobiol. A: Chem.* **366** 118
[40] Cao Y, Lei X Y, Chen Q L, Kang C, Li W X and Liu B 2018 *J J. Photochem. Photobiol. A: Chem.* **364** 794
[41] Yadav N G, Chaudhary L S, Sakhare P A, Dongale T D, Patil P S and Sheikh A D 2018 *J. Coll. Interface Scien.* **527** 289
[42] Nguyen T B, Huang C P and Doong R A 2018 *Scien. Total Environm.* **646** 745